ELSEVIER

Journal of Nuclear Materials 255 (1998) 44–58

journal of nuclear materials

On the mechanism of radiation-induced segregation in austenitic Fe–Cr–Ni alloys

T.R. Allen [a,*], J.T. Busby [a], G.S. Was [a], E.A. Kenik [b]

[a] *Department of Nuclear Engineering and Radiological Sciences, University of Michigan, Ann Arbor, MI 48109, USA*
[b] *Metals and Ceramics Division, Oak Ridge National Laboratory, Oak Ridge, TN 37831, USA*

Received 26 June 1997; accepted 23 December 1997

Abstract

The relative importance of the vacancy and interstitial contributions to radiation-induced segregation (RIS) in Fe–Cr–Ni alloys is studied to better understand the mechanisms causing changes in grain boundary composition and to improve the capability to predict RIS in austenitic Fe–Cr–Ni alloys. The primary driving mechanism for segregation in Fe–Cr–Ni alloys is shown to be the inverse Kirkendall (IK) mechanism, specifically the coupling between alloying elements and the vacancy flux. To study grain boundary segregation, seven alloys were irradiated with 3.2 MeV protons at temperatures from 200°C to 600°C and to doses from 0.1 to 3 dpa. Grain boundary compositions were measured using both Auger electron spectroscopy (AES) and scanning transmission electron microscopy with energy dispersive X-ray spectroscopy (STEM/EDS). Grain boundary compositions were compared to model predictions that assume segregation was driven either by preferential interaction of solute atoms with the vacancy flux alone or in combination with binding of undersized solutes to the interstitial flux. Calculations that assume the segregation is caused by preferential interaction of solute atoms with the vacancy flux generally followed the trends of the segregation measurements. However, the inclusion of interstitial binding to the IK model causes poor agreement between model predictions and segregation measurements, resulting in severe overprediction of Ni enrichment and Fe depletion. Comparisons of segregation models with RIS in alloys irradiated with neutrons also show that preferential interaction of solutes with the vacancy flux sufficiently describes segregation in Fe–Cr–Ni alloys.

1. Introduction

Radiation-induced segregation (RIS) is non-equilibrium segregation that occurs at point defect sinks during irradiation of an alloy at high temperature ($T_m = 0.3$ to 0.5) [1]. Radiation produces quantities of point defects far in excess of equilibrium concentrations. At high temperatures, these defects are mobile and travel to low energy sites such as surfaces, grain boundaries, dislocations, and other defect sinks. Segregation occurs when a given alloying component has a preferential association with the defect flux. Enrichment or depletion of each element occurs according to the relative interaction of each element with the defect flux. In irradiated austenitic Fe–Cr–Ni alloys, RIS causes Ni enrichment at grain boundaries and Cr depletion at grain boundaries. Fe either enriches or depletes depending on the bulk alloy composition. Because of the suspected link between grain boundary chromium depletion and irradiation-assisted stress corrosion cracking [2], an effort to better understand the mechanisms of RIS in Fe–Cr–Ni alloys is necessary.

Two mechanisms have been proposed as being significant contributors to RIS in Fe–Cr–Ni alloys. One is the preferential exchange of an alloying element with the vacancy flux resulting in a net solute flux toward or away from the boundary (the vacancy mechanism portion of the

* Corresponding author. Present address: Argonne National Laboratory-West, P.O. Box 2528, Idaho Falls, ID 83403-2528, USA.

0022-3115/98/$19.00
PII S0022-3115(98)00010-5

inverse Kirkendall effect). Preferential exchange of a solute with the vacancy flux as the sole contributor to RIS in Fe–Cr–Ni alloys was proposed by Marwick et al. [3] and modeled by Perks et al. [4]. The second mechanism is the preferential association of undersized atoms with the interstitial flux (interstitial binding). This interstitial binding mechanism was proposed by Wiedersich et al. [5] and extended to Fe–Cr–Ni alloys by Lam et al. [6]. In the interstitial binding model, both interstitial binding and preferential association of solutes with the vacancy flux contribute to the segregation.

Until recently, evidence identifying the primary driving mechanism for RIS in Fe–Cr–Ni alloys did not exist. The limited data on grain boundary segregation in irradiated Fe–Cr–Ni alloys has been insufficient to fully test the accuracy of the models. The dependence of RIS on irradiation temperature, dose, and alloy composition provide information about the segregation kinetics for a given alloy which can then be used to understand the operative segregation mechanism(s). Very few studies have systematically examined RIS in Fe–Cr–Ni alloys as a function of *either* temperature [7–9], dose [9–13], *or* alloy composition [13–15]. Bruemmer [16] used Ni-ion irradiation to study the dose and temperature dependence of RIS in alloys with a composition near 304 stainless steel. Damcott et al. [17,18] have analyzed a consistent set of RIS measurements in Fe-base alloys as a function of temperature, dose, and alloy composition. Simonen et al. [19] showed that for an Fe–21Cr–20Ni alloy, the segregation mechanism was preferential exchange of atoms with the vacancy flux. To determine if Simonen's conclusions are valid for Fe–Cr–Ni alloys in general, RIS measurements must be analyzed as a function of irradiation temperature, dose and alloy composition and compared to model calculations that assume a given segregation mechanism.

The focus of this study is the analysis and interpretation of RIS measurements from seven different Fe–Cr–Ni alloys, irradiated with protons at temperatures ranging from 200–600°C and to doses from 0.1 to 3.0 dpa, to determine the primary mechanism of segregation in austenitic Fe–Cr–Ni alloys under irradiation. This segregation data, along with segregation measurements from Fe–Cr–Ni alloys irradiated with neutrons, is analyzed in terms of the possible segregation mechanisms to determine if preferential association of solutes with the vacancy flux satisfactorily describes RIS in the Fe–Cr–Ni alloys studied or if the inclusion of interstitial binding is necessary to describe the measured segregation.

2. Experimental procedure

Grain boundary compositions have been measured in Ni–18Cr, Ni–18Cr–9Fe, Fe–20Cr–24Ni, and Fe–20Cr–9Ni alloys irradiated with protons. Grain boundary compositions previously reported by Damcott et al. [17,18] for Fe–16Cr–24Ni, Fe–20Cr–24Ni, Fe–24Cr–24Ni, and Fe–24Ni–19Cr, and by Carter et al. [20] for Fe–20Cr–9Ni are also included in this analysis. Table 1 gives the bulk compositions of these alloys as measured using electron microprobe analysis. Irradiations were conducted using 3.2 MeV protons at an ion flux of 6.25×10^{13} cm^{-2} s^{-1}, resulting in a nearly uniform damage rate of approximately 7×10^{-6} dpa/s through the first 35 μm of the proton range (45 μm). Details of the sample preparation procedure, irradiation technique, and grain boundary measurement techniques are given in Refs. [17,21]. A summary of the alloy-irradiation conditions on which grain boundary segregation measurements were made appears in Table 3. Unirradiated grain boundaries were characterized in the Ni–18Cr–9Fe, Ni–18Cr, and Fe–20Cr–9Ni alloys to determine the grain boundary composition prior to irradiation. The doses and dose rates reported throughout this paper are calculated using NRT [22] theory assuming a displacement energy of 25 eV.

Table 1
Summary of bulk alloy compositions in at.% (second line gives normalized compositions for Fe + Cr + Ni = 100%)

Alloy	Cr	Ni	Fe	Mn	Mo	Si	C	N	P	S
Fe–16Cr–24Ni	15.80	22.83	59.93	1.30	< 0.02	0.12	0.02	–	< 0.01	< 0.01
	16.03	23.16	60.81							
Fe–20Cr–24Ni	20.07	23.24	55.49	1.16	0.02	< 0.01	0.01	–	< 0.01	< 0.009
	20.31	23.52	56.17							
Fe–24Cr–24Ni	25.62	22.18	50.65	1.40	0.001	0.12	0.02	0.004	0.01	< 0.009
	26.02	22.53	51.45							
Fe–24Cr–19Ni	26.29	17.49	54.85	1.22	< 0.01	0.02	0.03	0.004	0.01	< 0.009
	26.66	17.73	55.61							
Fe–20Cr–9Ni	20.72	8.88	69.16	1.11	< 0.01	0.09	0.021	0.012	0.01	< 0.009
	20.97	8.99	70.04							
Ni–18Cr	18.24	81.74	0	0	0.002	0	0.005	–	0.006	0.004
	18.24	81.76	0							
Ni–18Cr–9Fe	18.26	72.36	9.32	0.010	0.002	0.027	0.014	–	0.007	0.004
	18.26	72.40	9.33							

Grain boundary microchemical analysis was performed using AES in a Perkin–Elmer PHI 660 Scanning Auger Microprobe and using STEM/EDS in a Phillips EM400T/FEG at Oak Ridge National Laboratory with an incident probe width of 2 nm. Details of the measurement techniques are given in Ref. [20].

Unless specifically noted in the text, model calculations were performed using the Perks et al. [4] model with the material parameters in Table 2. Model calculations are corrected for the fraction of point defects that escape the collision cascade and are free to migrate through the lattice [29]. A value of 0.2 was used as the freely migrating defect fraction for proton irradiations and a value of 0.02 for neutron irradiations (recognizing the fact that a greater number of defects created by neutrons recombine following cascade formation. One dpa of proton irradiation is equivalent to approximately 10 dpa of neutron irradiation). To correctly compare model calculations with experimental data, model calculations must properly account for the spatial resolution of the experimental measurement [20]. For instance, when measuring the grain boundary composition using AES, the Auger electrons that leave the sample and arrive at the detector originate not only from the grain boundary itself but also from atom planes adjacent to the grain boundary. Since the composition profile changes rapidly near the boundary, the contributions from atom planes adjacent to the grain boundary cause the AES measurement to be an underprediction of the actual segregation. Similarly, since the STEM electron probe has a finite width (about 2 nm entering the sample) and the total RIS profile width is on the order of 5–10 nm, STEM/EDS measurements average over a rapidly changing composition profile and also underpredict the actual segregation. To most accurately compare a model prediction with an experimental measurement, the model calculation must first be corrected for these analyzed volume effects.

To compare a model calculation with an AES measurement, the model calculation must be convoluted with the Auger electron escape depth. The escape depth describes the probability that an Auger electron emitted within a grain can escape the grain and reach the detector. Higher energy Auger electrons have larger escape depths and a greater probability of escape. The escape depth can be calculated from the empirical relationship [30]

$$\lambda_m = \frac{538}{E^2} + 0.41(aE)^{1/2}, \tag{1}$$

where the escape depth λ_m is expressed in monolayers. E is the energy (in eV) of the emitted Auger electron and a is the thickness of a monolayer (in nm). The monolayer thickness is calculated as follows:

$$a = \left[\left(\frac{A}{\rho n N}\right)10^{21}\right], \tag{2}$$

where A is the atomic or molecular weight (g/mole), ρ is the density (g/cm^3), n is the number of atoms in the molecule, and N is Avagadro's number. The escape depth is used in a broadening function (BF) of the form

$$\mathrm{BF} = \mathrm{e}^{-x/\lambda_m}, \tag{3}$$

which describes the probability of escape based on the depth x at which the Auger electron originated. The convolution of the calculated profile with the Auger electron broadening function is performed as follows:

$$C_{\mathrm{conv}} = \frac{\sum C(x)\mathrm{e}^{-x/\lambda_m}}{\sum \mathrm{e}^{-x/\lambda_m}}, \tag{4}$$

where $C(x)$ is the atomic concentration as a function of depth x (in nm).

Table 2
Inputs to the Perks' model

Input parameter	Notation	Value	Reference
Vacancy jump frequency for Fe	ω_{Fev}	2.8×10^{13} s^{-1}	[23]
Vacancy jump frequency for Cr	ω_{Crv}	5.0×10^{13} s^{-1}	[23]
Vacancy jump frequency for Ni	ω_{Niv}	1.5×10^{13} s^{-1}	[23]
Fe-vacancy correlation factor	f_{Fev}	0.785	[23]
Cr-vacancy correlation factor	f_{Crv}	0.668	[23]
Ni-vacancy correlation factor	f_{Niv}	0.872	[23]
Interstitial jump frequency	ω_{I}	1.5×10^{12} s^{-1}	[24]
Atom-interstitial correlation factor	f_{I}	0.44	[25]
Vacancy migration energy for Fe	$E_{\mathrm{vm}}^{\mathrm{Fe}}$	1.3 eV	[26]
Vacancy migration energy for Cr	$E_{\mathrm{vm}}^{\mathrm{Cr}}$	1.3 eV	[26]
Vacancy migration energy for Ni	$E_{\mathrm{vm}}^{\mathrm{Ni}}$	1.3 eV	[26]
Interstitial migration energy	E_{Im}	0.9 eV	[27]
Vacancy formation energy	E_{fv}	1.9 eV	[6]
Dislocation density	ρ	1×10^{14} m^2	[28]
Recombination volume	Z	12	FCC lattice
Thermodynamic factor	α	1	[6]

For a model calculation to be compared with a STEM/EDS measurement, the model calculation must be convoluted with the X-ray generation profile associated with the finite width electron beam. Typically, the beam is assumed to have a Gaussian shape described by a standard deviation σ, and scattering (beam broadening) is usually treated analytically or with a Monte Carlo simulation. The convolution of the model calculation with the X-ray generation profile is performed as follows:

$$(Ch)(x) = \int_{-\infty}^{\infty} C(x')h(x-x')\mathrm{d}x' \tag{5}$$

$$\int_{-\infty}^{\infty} h(x)\mathrm{d}x = 1, \tag{6}$$

where $C(x)$ is the model calculated profile, $h(x)$ is the X-ray generation function, and $(Ch)(x)$ is the convolution. This calculation is simplified by using the convolution theorem:

$$(\tilde{Ch}) = \tilde{C}(a)\tilde{h}(a), \tag{7}$$

which says that the Fourier transform of the convoluted profile $(\tilde{Ch})$ is equal to the product of the Fourier transform of the concentration profile, $\tilde{C}(a)$ and the Fourier transform of the X-ray generation function $\tilde{h}(a)$.

In all calculations, a constant sink density was used (1×10^{14} m^{-2}), consistent with the work of Perks et al. [4]. The sink density in unirradiated 304 L stainless steel is on the order of 10^{13} m^{-2} (network dislocation density 1.6×10^{13} m^{-2}) [28]. The sink density in 304 L stainless steel irradiated with protons at 400°C to 1 dpa is on the order of 10^{15} m^{-2} (network dislocation density 2.2×10^{14} m^{-2}, dislocation loop density 5.6×10^{21} m^{-3}, black dot density 6.7×10^{21} m^{-3}) [28]. For sink densities as large as 10^{15} m^{-2}, the calculated segregation at 400°C is relatively insensitive to changes in the sink density (the majority of point defects are lost due to mutual recombination). Since the majority of the segregation measurements in this study were taken on alloys irradiated to 1 dpa or less, 1×10^{14} m^{-2} is a reasonable estimate for the average sink density during the irradiation.

3. Results

Grain boundary composition measurements have been measured on seven different austenitic Fe–Cr–Ni alloys, irradiated at temperatures ranging from 200–600°C and to doses between 0.1 and 3.0 dpa. Over 1100 grain boundary measurements have been taken. Table 3 lists the average grain boundary compositions, along with the number of boundaries and samples analyzed, for each irradiation condition. The grain boundary composition measurements in Table 3 are as measured, with no attempt to deconvolute the measurements for beam effects. The values listed are normalized to Fe + Cr + Ni = 1.

The trends in the segregation measurements for a specific alloy as a function of dose and temperature are similar for both the AES and STEM/EDS measurements. The difference between the STEM/EDS and AES grain boundary measurements is between 2–3 at.% for Cr and between 1–5 at.% for Ni, which is expected and consistent with grain boundary concentrations measured in irradiated austenitic stainless steels using AES and STEM/EDS [12,20]. The consistency between the two independent measurements provides confidence that the measured trends are correct. In the following sections, the emphasis will be on a comparison between model calculations and AES measurements, but since the same trends are seen in the STEM/EDS measurements, the conclusions will hold for either type of measurement.

4. Determining the primary segregation mechanism

The segregation data can be analyzed to determine the primary RIS mechanism in Fe–Cr–Ni alloys. First, the relationships between diffusivities and self-diffusion coefficients, and migration energies and self-diffusion energies will be discussed. The direction of segregation (enrichment or depletion) of Fe, Cr, and Ni in each of the alloys is shown to be consistent with a vacancy mechanism. Next, a new variable that will be used to analyze the segregation, the 'Cr–Ni replacement rate,' is introduced. Then segregation measurements as a function of composition and temperature will be compared to model predictions that assume a vacancy mechanism to show that the segregation is consistent with an inverse Kirkendall mechanism-specifically a preferential association of solutes with the vacancy flux. The segregation in different alloys irradiated at 400°C to 1 dpa is analyzed to show that diffusivities do change with alloy composition and that the changes in diffusivity are consistent with changes in self-diffusion coefficients. Next, the segregation in alloys irradiated to 0.5 dpa at varying temperatures is analyzed to show that the variation in migration energy is also consistent with the variation in self-diffusion energy as composition changes. In every case, segregation is consistent with a vacancy mechanism. Segregation measurements are then compared to model predictions that assume an interstitial binding mechanism to show that the interstitial binding model poorly reproduces the measured segregation behavior. Finally, the unique segregation behavior of Fe in Fe–20Cr–9Ni is shown to be predicted by a vacancy mechanism but not by the interstitial binding mechanism.

4.1. Relationship between diffusivities and self-diffusion coefficients

Radiation-induced segregation occurs when a local point defect flux causes a net flux of atoms toward or away from

Table 3
Summary of segregation measurements (uncertainty given by the standard deviation of the mean ($\sigma/\sqrt{N}$)

Alloy	Temp. (°C)	Dose (dpa)	Fe (at.%)	Cr (at.%)	Ni (at.%)	Measurements	Samples	Irradiations
AES								
Ni–18Cr	200	0.5	–	14.6 ± 0.2	85.4 ± 0.2	28	2	1
Ni–18Cr	300	0.5	–	11.5 ± 0.2	88.5 ± 0.2	33	2	1
Ni–18Cr	400	0.5	–	10.1 ± 0.2	89.9 ± 0.2	62	5	3
Ni–18Cr	500	0.5	–	12.9 ± 0.5	87.1 ± 0.5	23	2	1
Ni–18Cr–9Fe	200	0.5	6.7 ± 0.5	15.7 ± 0.2	77.6 ± 0.5	16	1	1
Ni–18Cr–9Fe	300	0.5	5.4 ± 0.5	13.8 ± 0.3	80.8 ± 0.6	14	1	1
Ni–18Cr–9Fe	400	0.5	5.8 ± 0.3	13.5 ± 0.2	80.7 ± 0.5	27	2	1
Ni–18Cr–9Fe	500	0.5	6.5 ± 0.3	15.7 ± 0.2	77.8 ± 0.5	30	2	1
Ni–18Cr	–	0.0	–	17.1 ± 0.2	82.9 ± 0.2	12	1	NA
Ni–18Cr	400	0.1	–	13.4 ± 0.3	86.6 ± 0.3	33	2	1
Ni–18Cr	400	0.3	–	11.8 ± 0.2	88.2 ± 0.2	32	2	1
Ni–18Cr	400	1.0	–	10.6 ± 0.3	89.4 ± 0.3	36	2	2
Ni–18Cr–9Fe	–	0.0	9.4 ± 0.3	18.0 ± 0.4	72.6 ± 0.5	12	2	–
Ni–18Cr–9Fe	400	0.1	5.2 ± 0.2	13.9 ± 0.2	80.9 ± 0.3	23	2	1
Ni–18Cr–9Fe	400	0.3	4.9 ± 0.3	13.9 ± 0.4	81.1 ± 0.4	23	2	1
Ni–18Cr–9Fe	400	1.0	5.5 ± 0.3	13.8 ± 0.3	80.7 ± 0.6	27	2	2
Fe–20Cr–9Ni	–	0.0	68.7 ± 0.3	23.2 ± 0.4	8.1 ± 0.1	12	1	–
Fe–20Cr–9Ni	400	0.1	69.4 ± 0.2	21.4 ± 0.3	9.2 ± 0.2	25	3	1
Fe–20Cr–9Ni	400	1.0	70.3 ± 0.2	17.0 ± 0.2	12.7 ± 0.2	65	5	3
Fe–20Cr–9Ni	400	3.0	66.4 ± 0.4	9.0 ± 0.4	24.6 ± 0.6	24	2	1
Fe–20Cr–24Ni	200	1.0	53.5 ± 0.8	20.8 ± 0.6	25.8 ± 0.8	11	1	1
Fe–20Cr–24Ni	300	0.5	53.7 ± 0.6	19.3 ± 0.7	27.0 ± 0.4	33	3	1
Fe–20Cr–24Ni	400	0.5	52.0 ± 1.0	13.6 ± 0.3	34.5 ± 1.0	21	2	1
Fe–20Cr–24Ni	500	0.5	48.4 ± 1.2	13.0 ± 0.9	38.6 ± 0.5	36	3	1
Fe–20Cr–24Ni	600	0.5	55.2 ± 0.4	17.9 ± 0.3	26.8 ± 0.5	27	2	1
Fe–20Cr–24Ni	400	0.1	55.2 ± 0.3	18.0 ± 0.2	26.9 ± 0.3	35	2	1
Fe–20Cr–24Ni	400	1.0	51.9 ± 0.7	12.1 ± 0.4	36.0 ± 0.8	38	3	2
Fe–20Cr–24Ni	400	3.0	47.6 ± 0.9	14.1 ± 0.6	38.4 ± 1.1	39	3	1
Fe–16Cr–24Ni	400	1.0	50.5 ± 0.7	10.7 ± 0.4	38.9 ± 1.0	27	3	2
Fe–24Cr–24Ni	400	1.0	49.8 ± 0.5	14.7 ± 0.5	35.4 ± 0.7	36	3	2
Fe–24Cr–19Ni	400	1.0	57.1 ± 0.4	17.2 ± 0.7	25.7 ± 0.4	23	2	1
STEM								
Ni–18Cr	–	0.0	–	18.8 ± 0.2	81.2 ± 0.2	15	1	–
Ni–18Cr	400	0.1	–	15.7 ± 0.2	84.3 ± 0.2	22	2	2
Ni–18Cr	400	0.3	–	14.3 ± 0.3	85.7 ± 0.3	34	2	1
Ni–18Cr	400	0.5	–	13.0 ± 0.3	87.0 ± 0.3	33	2	2
Ni–18Cr	400	1.0	–	13.6 ± 0.3	86.4 ± 0.3	15	1	1
Ni–18Cr–9Fe	–	0.0	9.2 ± 0.1	17.9 ± 0.2	72.8 ± 0.2	17	1	–
Ni–18Cr–9Fe	400	0.1	6.6 ± 0.1	16.0 ± 0.2	77.4 ± 0.3	22	2	1
Ni–18Cr–9Fe	400	0.3	5.8 ± 0.1	15.4 ± 0.2	78.7 ± 0.2	18	1	1
Ni–18Cr–9Fe	400	0.5	5.4 ± 0.1	14.4 ± 0.2	80.2 ± 0.3	45	2	1
Ni–18Cr–9Fe	400	1.0	5.8 ± 0.2	15.3 ± 0.2	78.7 ± 0.3	20	1	1
Fe–20Cr–9Ni	–	0.0	69.5 ± 0.1	21.3 ± 0.1	9.2 ± 0.0	23	1	–
Fe–20Cr–9Ni	400	0.1	70.4 ± 0.1	20.0 ± 0.1	9.6 ± 0.1	23	1	1
Fe–20Cr–9Ni	400	0.5	70.6 ± 0.2	19.1 ± 0.2	10.3 ± 0.2	29	1	1
Fe–20Cr–9Ni	400	1.0	71.8 ± 0.1	17.2 ± 0.2	11.0 ± 0.2	26	1	1
Fe–20Cr–9Ni	400	3.0	70.6 ± 0.8	13.9 ± 0.3	15.5 ± 0.8	16	1	1
Fe–20Cr–24Ni	–	0.0	56.1 ± 0.1	20.3 ± 0.1	23.6 ± 0.1	20	1	–
Fe–20Cr–24Ni	400	0.5	52.9 ± 0.5	14.2 ± 0.3	32.9 ± 0.7	10	1	1
Fe–20Cr–24Ni	400	1.0	50.7 ± 0.5	14.0 ± 0.2	35.3 ± 0.7	50	2	2
Fe–20Cr–24Ni	400	3.0	51.9 ± 0.3	14.6 ± 0.1	33.5 ± 0.4	30	2	1

the grain boundary. Segregation can be caused by preferential interactions of atoms with the vacancy flux. This atom flux depends on the diffusivity of each constituent (which describes the rate at which an atom will interact with the point defect flux) and on the local composition. For example, the flux of Cr atoms due to interaction with the vacancy flux is a function of the local Cr concentration, C_{Cr}, and the Cr vacancy diffusivity, d_{Crv}:

$$J_j v^{Cr} = f(C_{Cr}, d_{Crv}). \tag{8}$$

Therefore, if *either* the concentration or the diffusivity changes, the flux, and therefore the amount of segregation, will change. As shown below, vacancy diffusivities are directly related to self-diffusion coefficients which are measured in high temperature diffusion experiments where the diffusion is driven strictly by vacancy motion. Consequently, changes in diffusivity as a function of alloy composition can be compared to changes in self-diffusion coefficients as a function of alloy composition to provide evidence that segregation in Fe–Cr–Ni alloys is driven by a vacancy mechanism.

The relationship between the diffusivity and the self-diffusion coefficient is given by

$$D_{vsd}^{Cr} = C_v d_{Crv} = C_v d_0^{Cr} \exp\left(\frac{-E_{vm}^{Cr}}{kT}\right) = D_0^{Cr} \exp\left(\frac{-E_{vsd}^{Cr}}{kT}\right), \tag{9}$$

where D_{vsd}^{Cr} is the self-diffusion coefficient, C_v is the vacancy concentration, and d_{Crv} is the Cr-vacancy exchange diffusivity. The diffusivity is a material property and is described with two components, a temperature independent pre-exponential term d_0^{Cr} and a migration energy term E_{vm}^{Cr}:

$$d_{Crv} = d_0^{Cr} \exp\left(\frac{-E_{vm}^{Cr}}{kT}\right). \tag{10}$$

The self-diffusion coefficient also consists of a pre-exponential factor D_0^{Cr} and a self-diffusion energy term E_{sd}^{Cr}.

The ratio of the atom-vacancy diffusivities, d_{Av}/d_B, is equal to the ratio of the self-diffusion coefficients D_{vsd}^{A}/D_{vsd}^{B}. The relationship between self-diffusion energy and migration energy is given by

$$E_{sd} = E_{vm} + E_{vf}, \tag{11}$$

where E_{vf} is the vacancy formation energy which determines the vacancy concentration. The vacancy concentration in unirradiated materials increases with temperature. Therefore, as temperature increases, the self-diffusion coefficient increases because the diffusivity increases and the concentration of vacancies increases. In irradiated alloys, at the temperatures at which RIS occurs, the majority of the vacancies are created by displacement damage and thermally generated vacancies are a negligible contribution to the total vacancy concentration. *Any changes in the diffusivity due to changes in material properties are reflected in the self-diffusion coefficient.*

If a change in alloy composition causes the diffusivity pre-exponential factor to increase, the self-diffusion coefficient pre-exponential factor will also increase. If change in alloy composition causes the migration energy to increase, the self-diffusion energy will also increase. Therefore, if the variations of diffusivity and migration energy with changing composition follow the variation of the self-diffusion coefficient and self-diffusion energy with changing composition, the segregation is consistent with a vacancy mechanism.

Diffusivities also describe the motion of interstitials in irradiated alloys. The interstitial diffusivities describe the rate of interaction of atoms with the interstitial flux and are of the form

$$d_i^{Cr} = d_0^{Cr,i} \exp\left(\frac{-E_{im}^{Cr}}{kT}\right). \tag{12}$$

Unlike vacancies, the diffusivities of interstitials cannot be measured in a thermal diffusion experiment. The formation energy of interstitials is large so the concentration of thermally generated interstitials is negligible.

4.2. Direction of segregation and the relationship to a vacancy mechanism

The equations describing RIS have been solved by Wiedersich et al. [5] to describe the relationship between an atom gradient and the vacancy gradient at steady-state for a binary alloy. The ratio of these two gradients has been termed the determinant (M) by Watanabe and Takahashi [31]. For a binary alloy, the determinant for atom A is

$$M_A = \frac{\nabla C_A}{\nabla C_v} = \frac{C_A C_B d_{Ai} d_{Bi}}{\alpha(d_{Bi} C_B D_A + d_{Ai} C_A D_B)} \left(\frac{d_{Av}}{d_{Ai}} - \frac{d_{Bv}}{d_{Bi}}\right). \tag{13}$$

If the term $((d_{Av}/d_{Ai}) - (d_{Bv}/d_{Bi}))$ is positive, the gradient of atom A is in the same direction as the vacancy gradient and atom A would deplete. Watanabe and Takahashi [31] derived an expression for the determinant in a ternary alloy. The determinant for atom j is

$$M_j = \frac{\nabla C_j}{\nabla C_v} = \frac{\dfrac{d_{jv} C_j}{D_j} \sum\limits_{k \neq j} \dfrac{d_{ki} C_k}{D_k} - \dfrac{d_{ji} C_j}{D_j} \sum\limits_{k \neq j} \dfrac{d_{kv} C_k}{D_k}}{\alpha \sum\limits_k \dfrac{d_{ki} C_k}{D_k}}. \tag{14}$$

If the determinant for the jth atom is positive, then the jth atom depletes during irradiation.

Table 4(a) shows the Cr, Fe, and Ni determinants calculated for all seven alloys *assuming that preferential*

Table 4
(a) Segregation behavior in Ni–18Cr, Ni–18Cr–9Fe, Fe–20Cr–9Ni, Fe–16Cr–24Ni, Fe–20Cr–24Ni, Fe–24Cr–24Ni, and Fe–24Cr–19Ni compared to inverse Kirkendall predictions. Determinants (M) calculated using Eq. (14)

Alloy	M_{Cr}	M_{Fe}	M_{Ni}	Cr	Fe	Ni	Analysis method
Ni–18Cr	3.9	–	−3.9	Depletes	–	Enriches	AES
Ni–18Cr	3.9	–	−3.9	Depletes	–	Enriches	STEM/EDS
Ni–18Cr–9Fe	5.0	0.4	−5.4	Depletes	Depletes	Enriches	AES
Ni–18Cr–9Fe	5.0	0.4	−5.4	Depletes	Depletes	Enriches	STEM/EDS
Fe–20Cr–9Ni	5.0	−3.0	−2.0	Depletes	Enriches	Enriches	AES
Fe–20Cr–9Ni	5.0	−3.0	−2.0	Depletes	Enriches	Enriches	STEM/EDS
Fe–16Cr–24Ni	4.0	3.6	−7.6	Depletes	Depletes	Enriches	AES
Fe–20Cr–24Ni	5.0	2.4	−7.4	Depletes	Depletes	Enriches	AES
Fe–20Cr–24Ni	5.0	2.4	−7.4	Depletes	Depletes	Enriches	STEM/EDS
Fe–24Cr–24Ni	6.0	0.6	−6.6	Depletes	Depletes	Enriches	AES
Fe–24Cr–19Ni	6.5	−1.8	−4.7	Depletes	Enriches	Enriches	AES

(b) Diffusivity ratios used to calculate determinants (M) in (a)

Alloy	d_{vm}^{Cr}	d_{vm}^{Fe}	d_{vm}^{Ni}	Ref.
Ni–18Cr	1.65	–	1.00	[32]
Ni–18Cr–9Fe	2.00	1.20	1.00	[33]
Fe–16Cr–24Ni	2.55	1.69	1.00	[23]
Fe–20Cr–24Ni	2.48	1.61	1.00	[23]
Fe–24Cr–24Ni	2.39	1.47	1.00	[23]
Fe–24Cr–19Ni	2.33	1.35	1.00	[23]
Fe–20Cr–9Ni	2.31	1.28	1.00	[23]

coupling with the vacancy flux causes the segregation. The determinants were calculated using the vacancy diffusivities in Table 4(b). The interstitial diffusivities were assumed equal for Cr, Fe, and Ni. The segregation trends (enriching or depleting at the grain boundary) for Cr, Fe, and Ni that were seen in the RIS measurements are also listed. For each alloy where the Cr determinant is positive Cr depletes, where the Ni determinant is negative Ni enriches, where the Fe determinant is positive Fe depletes, and where the Fe determinant is negative Fe enriches. The experimental segregation measurements are all consistent with a vacancy mechanism.

4.3. Measuring segregation: Cr–Ni replacement rate

To study segregation as a function of alloy composition, a variable is introduced to relate the amount of segregation to the relative diffusivities of Fe, Cr, and Ni [34]. This variable is the ratio of the *magnitude* of the change in Cr concentration (unirradiated grain boundary Cr minus irradiated grain boundary Cr) to the *magnitude* of the change in Ni concentration (unirradiated grain boundary Ni minus irradiated grain boundary Ni) ($|\Delta Cr/\Delta Ni|$) and is termed the 'Cr–Ni replacement rate,' designated as $R^{Cr \to Ni}$. This ratio gives the fraction of grain boundary sites occupied by Ni that were previously occupied by Cr. A ratio of 1 indicates that every Cr that leaves the boundary is replaced by a Ni (with Fe neither enriching or depleting). A value of 0.5 indicates that for two Ni atoms arriving at the boundary, one Cr leaves (and therefore one Fe leaves) to conserve matter. The segregation could also be described using the 'Fe-Ni replacement rate' ($|\Delta Fe/\Delta Ni|$), which is related to the Cr–Ni replacement rate by

$$Cr + Fe + Ni = 1 \text{ or } \frac{\Delta Cr}{\Delta Ni} + \frac{\Delta Fe}{\Delta Ni} = -1. \quad (15)$$

However, the Cr–Ni replacement rate was chosen to analyze segregation data because Cr always depletes and Ni always enriches in Fe–Cr–Ni alloys. Additionally, the changes in concentration from bulk to grain boundary are greatest for Cr and Ni and therefore the largest changes are captured using $|\Delta Cr/\Delta Ni|$.

The Cr–Ni replacement rate is determined by the relative amounts of grain boundary segregation. The kinetics of segregation in an Fe–Cr–Ni system are determined by the ratios of the diffusivities d_{vm}^{Cr}/d_{vm}^{Ni}, d_{vm}^{Fe}/d_{vm}^{Ni}, and d_{vm}^{Cr}/d_{vm}^{Fe}. Therefore, if the segregation is driven by the vacancy flux, Cr must be the fastest diffuser and Ni the slowest diffuser in the system

$$\frac{d_{vm}^{Cr}}{d_{vm}^{Ni}} > \frac{d_{vm}^{Fe}}{d_{vm}^{Ni}} > 1 \quad (16)$$

Fe will enrich or deplete depending on the Fe diffusivity relative to the average diffusivity in the alloy. If the Fe diffusivity is greater than the average diffusivity in the alloy, Fe will deplete. If the Fe diffusivity is less than the average diffusivity in the alloy, Fe will enrich. The Ni

enriched at the boundary occupies positions previously occupied by either Cr or Fe. The amount of Cr and Fe depletion is therefore determined by the Cr/Fe diffusivity ratio d_{vm}^{Cr}/d_{vm}^{Fe}.

Fig. 1 demonstrates the effect of relative diffusivity on grain boundary segregation. Perks model predictions for the grain boundary Cr concentration are plotted against model-predicted grain boundary Ni concentration for an Fe–20Cr–24Ni alloy irradiated at 400°C to various doses. As the dose increases, the grain boundary Cr depletes and the grain boundary Ni enriches. Five different calculations are shown, each assuming a different ratio of the Cr to Fe diffusivity (d_{vm}^{Cr}/d_{vm}^{Fe}). As the Cr to Fe diffusivity increases from 1.3 to 2.1, the change in grain boundary Cr concentration (ΔCr) increases and the change in grain boundary Ni concentration (ΔNi) decreases. Therefore, the Cr–Ni replacement rate ($R^{Cr\rightarrow Ni} = |\Delta Cr/\Delta Ni|$) increases as the Cr to Fe diffusivity increases. The Cr–Ni replacement rate is thus a measure of the relative diffusivities.

Simonen et al. [19] have previously used the terms 'diffusion path' and 'kinetic opportunity' to describe the segregation process in ternary alloys. The diffusion path is determined by relative diffusivities (the paths in Fig. 1). The kinetic opportunity determines how far along the diffusion path the compositions change and is determined by the dose, temperature, and the position (distance from the grain boundary) at which the segregation is measured. Replacement rate is a comparison of the diffusion paths of different alloys with the same kinetic opportunity (same dose, temperature and measurement location). Since the diffusion path is determined by relative diffusivities, comparison of replacement rates allows a comparison of diffusivities between different alloys.

4.4. Composition dependence of RIS and its relationship to a vacancy mechanism

In a previous work, ratios of diffusivities inferred from RIS measurements have been compared to ratios of high temperature diffusion coefficients to show that RIS is consistent with a vacancy mechanism [34]. In this section, a summary of that work is presented. RIS measurements from Fe-base alloys irradiated at 400°C to 1 dpa are compared to model calculations. Two sets of model calculations are performed. One set uses ratios of diffusivities calculated from ratios of high temperature diffusion coefficients. These ratios vary with alloy composition. The second set of model calculations serves as a reference and assumes that the diffusivities for Fe, Cr, and Ni do not change with alloy composition (the diffusivities for Fe–15Cr–20Ni are used). For each alloy, the Cr–Ni replacement rate is calculated from measurements and model calculations. If the measured Cr–Ni replacement rates are consistent with model predictions which use ratios of diffusivities calculated from high temperature diffusion coefficients (which are driven only by vacancy flux), then RIS is driven primarily by a vacancy mechanism. If the measured segregation is inconsistent with model predictions that use diffusivities calculated from high temperature diffusion measurements, then either the relative diffusivities of Cr, Ni, and Fe are different at irradiation temperatures, or a significant contribution to the segrega-

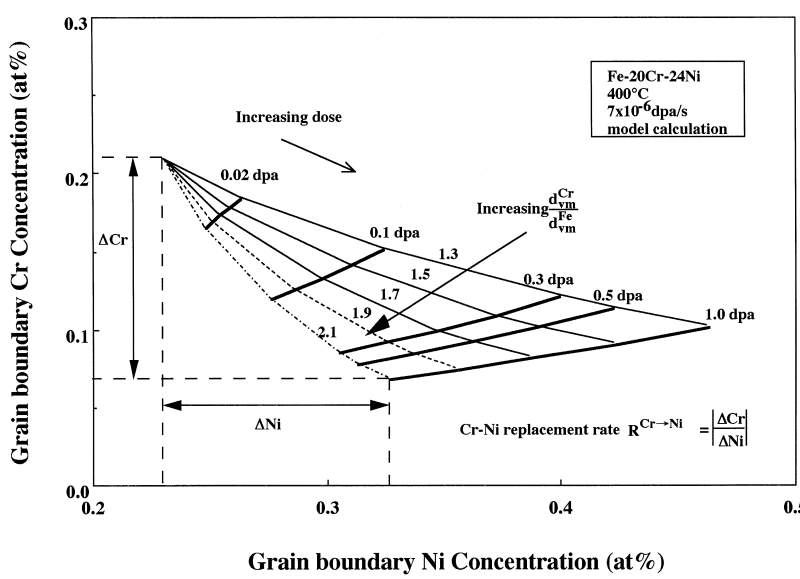

Fig. 1. Model calculations indicate how changing diffusivities alter the predicted segregation. Increasing the Cr–Fe diffusivity ratio increases the Cr depletion and decreases the Ni enrichment.

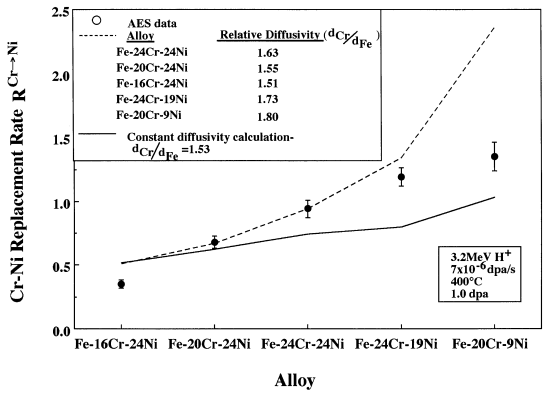

Fig. 2. Comparison of model predicted and measured segregation. Calculations using diffusivities based on self-diffusion coefficients predict the trends of the segregation.

tion comes from differences in solute coupling with the interstitial flux.

Fig. 2 shows the results of this comparison. Cr–Ni replacement rates calculated from segregation data are compared to Cr–Ni replacement rates calculated from model predictions using the Perks model [4], which assumes that only the vacancy flux contributes to the grain boundary segregation (no differences in interstitial jump rates). Constant diffusivity ratios of $d_{vm}^{Cr}/d_{vm}^{Ni} = 2.55$, $d_{vm}^{Fe}/d_{vm}^{Ni} = 1.67$ and $d_{vm}^{Cr}/d_{vm}^{Fe} = 1.53$ are used for the constant diffusivity calculations for all alloys (other inputs are given in Table 2). These diffusivity ratios are based on the diffusion coefficient ratios measured by Rothman et al. [23] for an Fe–15Cr–20Ni alloy and have traditionally been used in RIS calculations for stainless steels. Alloy specific diffusivities, interpolated (Fe–16Cr–24Cr, Fe–20Cr–24Ni, Fe–24Cr–24Ni, and Fe–24Cr–19Ni) and extrapolated (Fe–20Cr–9Ni) from diffusion coefficients (D_{Cr}/D_{Fe}) from Rothman et al. [23] are used for the variable diffusivity calculations and are listed in Fig. 2 for reference. As shown, the trends of the segregation measurements are better predicted from the calculations using the alloy specific diffusivities. Since the observed diffusivities in the Fe-base alloys are consistent with high temperature diffusion coefficient measurements, the primary driving force for segregation is a coupling with the vacancy flux.

4.5. Temperature dependence of RIS and its relationship to a vacancy mechanism

The temperature dependence of RIS is alloy specific and has previously been shown to be consistent with a vacancy mechanism [34]. The temperature dependence of the segregation is determined by the migration energies, which can be determined for each alloy. If segregation is measured in two alloys with different Cr-vacancy migration energies, the alloy with the smaller migration energy will have its maximum segregation at a lower temperature. These migration energies can then be compared to self-diffusion energies to show that segregation is consistent with a vacancy mechanism.

The segregation behavior as a function of temperature is plotted for Ni–18Cr, Ni–18Cr–9Fe, and Fe–20Cr–24Ni in Fig. 3. The minimum grain boundary Cr concentration occurs at the highest temperature in the Fe–20Cr–24Ni alloy and at the lowest temperature in the Ni–18Cr–9Fe alloy. From the RIS data, we would expect the migration energy to be largest in Fe–20Cr–24Ni and smallest in the Ni–18Cr–9Fe. Since self-diffusion energies are the sum of the vacancy migration energy and the bulk vacancy formation energy ($E_{sd} = E_{vm} + E_{vf}$), self-diffusion energies can be used as a guide in determining vacancy migration energies.

The measured self-diffusion energies (E_{sd}^{Cr}) for Cr for each alloy are compared in Fig. 3. The Fe–20Cr–24Ni data is interpolated from the data of Rothman et al. [23] and the Ni-base data is interpolated from the data of Million et al. [33], and Ruzickova and Million [32]. Data are used from three different experiments because the ranges of alloy composition measured are non-overlapping. Rothman's measurements cover 15–22 wt% Cr and 20–45 wt% Ni. Million's data covers 0–30.4 wt% Cr and 15.5–78.7 wt% Ni. The measurements only overlap at one data point (approximately 20Cr–45Ni) where both give similar self-diffusion energies for Cr (3.04 eV). Ruzickova and Million measured self-diffusion in binary Ni–Cr alloys. As shown, the self-diffusion of Cr is largest in the alloys with the higher temperature of minimum segregation. For the alloys used in this segregation study, the smallest vacancy migration energy and thus the fastest segregation is expected in the Ni–18Cr–9Fe alloy. Since the segregation behavior is consistent with trends predicted by self-diffu-

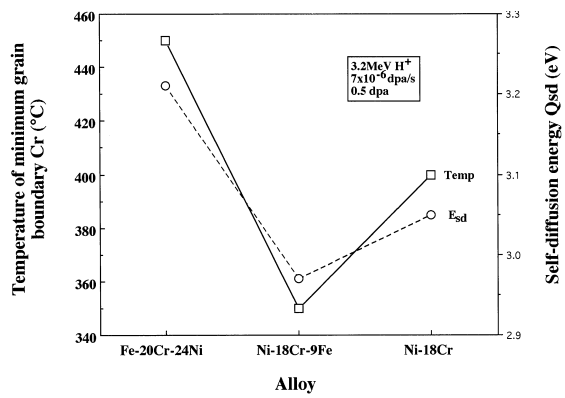

Fig. 3. Trends in minimum Cr segregation temperature correspond with trends in self-diffusion energy. The segregation is consistent with the segregation being driven by preferential association of solutes with the vacancy flux.

sion energy (a function of interactions with vacancies), the temperature dependence of RIS is consistent with a vacancy effect.

4.6. Comparison of interstitial binding predictions to measured segregation

Although considerable evidence has been presented that indicates preferential interaction with the vacancy flux is the primary mechanism of RIS in Fe–Cr–Ni alloys, a more direct test of interstitial binding is required. Lam et al. [6,35] proposed that interstitial binding was an important factor in describing RIS in Fe–Cr–Ni alloys. Specifically, Ni, as an undersized element should interact preferentially with the interstitial flux. To link Ni atoms to the interstitial flux, a binding energy in the interstitial diffusivities was included to represent the non-random occupation of interstitials by a given element:

$$C_{\mathrm{Ni}}^{\mathrm{i}} = C_{\mathrm{i}} \frac{C_{\mathrm{Ni}} \exp\left(\frac{H_{\mathrm{Ni,i}}^{b}}{kT}\right)}{C_{\mathrm{Ni}} \exp\left(\frac{H_{\mathrm{Ni,i}}^{b}}{kT}\right) + C_{\mathrm{Fe}} \exp\left(\frac{H_{\mathrm{Fe,i}}^{b}}{kT}\right) + C_{\mathrm{Cr}} \exp\left(\frac{H_{\mathrm{Cr,i}}^{b}}{kT}\right)} \tag{17}$$

A positive binding energy for Ni causes Ni to preferentially interact with the interstitial flux. In Lam's model, the input parameters are similar to those in Table 2, with the exception that Lam used 0.3 eV for the interstitial migration energy for Fe and Cr, 0.9 eV for the interstitial migration energy of Ni, and 1.0 eV for the interstitial binding energy for Ni. The interstitial migration energy of 0.3 eV used for Fe and Cr corresponds to the migration energy of self-interstitials in Fe [36]. The interstitial migration energy of 0.9 eV for Ni corresponds to the experimental value of the interstitial migration energy in Fe–16Cr–25Ni [37]. The interstitial binding energy of 1.0 eV for Ni is typical for di-interstitials in an fcc lattice [38]. The interstitial binding for Cr and Fe were assumed to be negligible and were set to zero. Lam's formulation for RIS has been used to calculate the expected segregation in Fe–20Cr–24Ni. Model calculations are compared to the segregation measurements from Fe–20Cr–24Ni as a function of temperature in Fig. 4. Because the interstitial binding term affects the Ni-interstitial concentration exponentially with temperature, the segregation behavior as a function of temperature provides the best test of the interstitial binding theory. In addition to the predictions using Lam's model, predictions from the Perks model (vacancy mechanism only) are included in the figure for comparison. Fig. 4 clearly shows that the interstitial binding model severely overpredicts the measured segregation. The overprediction is especially evident for the Ni segregation where the interstitial binding model predicts segregation of

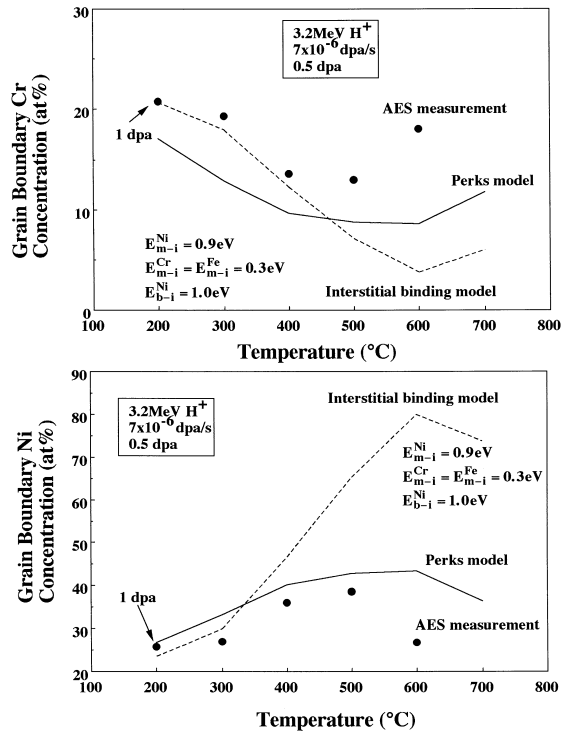

Fig. 4. Grain boundary Cr and Ni concentration in Fe–20Cr–24Ni, measured using AES and plotted as a function of temperature. Measurements are compared to model calculations using the Perks model and to the interstitial binding model. Perks model calculations use the inputs from Table 2. For the interstitial binding model calculations, the interstitial migration and binding energies are listed.

up to 80 at.% Ni for a 600°C irradiation. The segregation measurements do not approach these values.

While the interstitial binding model does not work for this set of input parameters, a more thorough test of the model over a range of reasonable migration and binding energies is required. The input parameters used in Fig. 4 assumed that Fe and Cr migrated as self-interstitials with a low migration energy of 0.3 eV, while Ni preferentially migrated with Fe as an Fe–Ni dumbbell with a larger migration energy of 0.9 eV. As a first test of the sensitivity of the model to the binding energy, a set of calculations is performed which assumes equal migration energies for Fe, Cr, and Ni interstitials. The migration energy of interstitials is set to 0.9 eV (corresponding to the measured value in Fe–16Cr–25Ni during annealing following neutron irradiation). The binding energy of Ni-interstitials is varied from 0.1 eV (a value much lower than measured for di-interstitials in FCC alloys) to 1.0 eV (a value typical for di-interstitials in FCC alloys). The results of the calculations are shown in Fig. 5.

For binding energies as small as 0.1 eV, the interstitial binding model overpredicts the segregation to a much

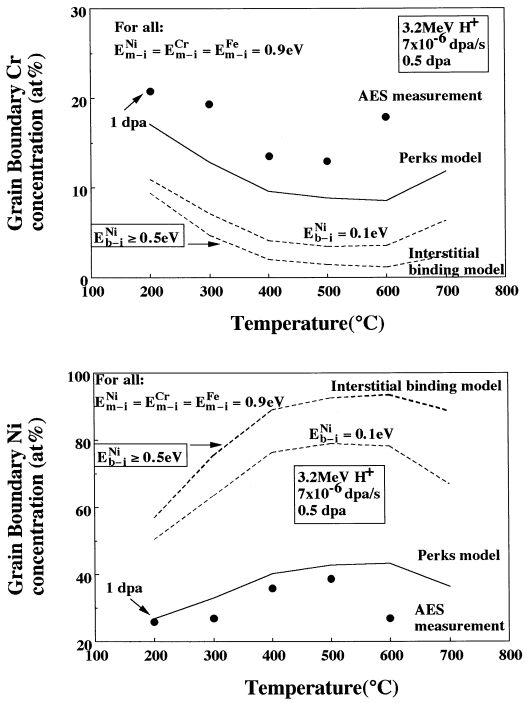

Fig. 5. Grain boundary Cr and Ni concentration in Fe–20Cr–24Ni, measured using AES and plotted as a function of temperature. Measurements are compared to model calculations using the Perks model and to the interstitial binding model. Perks model calculations use the inputs from Table 2. For the interstitial binding model calculations, the interstitial migration and binding energies are listed.

greater extent than does the Perks model. 'Since the Perks (vacancy effects only) model overpredicts the Ni enrichment, any binding of Ni to the interstitial flux will make the overprediction greater'. At binding energies of 0.5 eV and higher, the interstitial binding model calculation is insensitive to the binding energy and greatly overpredicts the segregation. This observation is similar to that of Lam who found that in calculating the segregation in proton irradiated Fe–Cr–Ni alloys, the segregation is insensitive to binding energies within the range of 0.9–1.5 eV [35]. Eq. (17) can be analyzed to show that the interstitial binding model should indeed be insensitive to binding energies in this range. For Ni-interstitial binding energies of 0.5 eV, the concentration of interstitials that are Ni atoms at 400°C, C^i_{Ni}, is 99 at.%. Larger values of the Ni-interstitial binding energy cannot significantly increase the concentration of interstitials that are Ni. This set of calculations indicate that the introduction of interstitial binding as a significant factor in the segregation process causes the model to predict much greater segregation than occurs.

A final check of the interstitial binding model returns to the condition used in the calculations for Fig. 4 in which Fe and Cr self-interstitials migrate at a much lower energy than do Ni dumbbells. As dumbbells, the Ni interstitials must rotate prior to diffusing, and therefore migrate at a higher energy. This higher migration energy could compensate for the preferential association of Ni to interstitials, reducing the Ni flux to the grain boundary, resulting in model predictions closer to experimental data. It has already been shown that if the Fe and Cr migration energy is 0.3 eV, the Ni migration energy is 0.9 eV, and the Ni-interstitial binding energy is 1.0 eV, the interstitial binding model severely overpredicts the segregation. In addition, it has been shown that the interstitial binding model is insensitive to binding energies greater than 0.5 eV. The final test was to set the Ni-interstitial binding energy to 1.0 eV, the Fe and Cr interstitial migration energies to 0.3 eV and increase the Ni-interstitial migration energy above 0.9 eV until a reasonable match with the experimental data was found. Then, the best fit Ni-interstitial migration energy can be compared to the experimental uncertainty in the measured interstitial migration energy in Fe–16Cr–25Ni, which is 0.89 ± 0.06 eV [37].

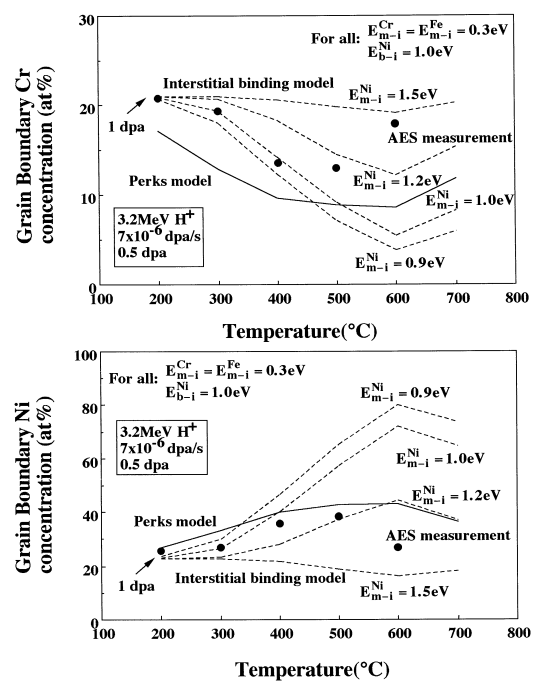

Fig. 6. Grain boundary Cr Ni concentration in Fe–20Cr–24Ni measured using AES and plotted as a function of temperature. Measurements are compared to model calculations using the Perks model and to the interstitial binding model. Perks model calculations use the inputs from Table 2. For the interstitial binding model calculations, the interstitial migration and binding energies are listed.

Fig. 6 shows the results of these calculations. At a Ni-interstitial migration energy of 1.0 eV, the interstitial binding model still severely overpredicts the segregation. At a Ni-interstitial migration energy of 1.2 eV, the interstitial binding model and the Perks model predict the measured segregation with similar accuracy. At 1.5 eV, the interstitial binding model predicts little segregation at all. The 'best fit' occurs with a Ni-interstitial migration energy of around 1.2 eV. However, this energy is well outside the range of the measured interstitial migration energy for a similar alloy (0.83–0.95 eV). Even allowing only Ni atoms to migrate at the higher migration energy (and keeping Fe and Cr interstitials at a small migration energy), the interstitial binding model cannot accurately predict the measured segregation unless unrealistic input parameters are used.

Fig. 7 plots the model predicted grain boundary Ni concentration vs. the measured Ni concentration for the five different Fe-base alloys in this study using both the Perks (inverse Kirkendall preferential vacancy effects) and the interstitial binding models. While the Perks (vacancy effects) model tends to follow the trends of the measured segregation, the interstitial binding model overpredicts the measured compositions by a large margin. The temperature dependent interstitial binding model (Eq. (17)) severely overpredicts the segregation and is unlikely to occur in Fe–Cr–Ni alloys. These calculations do not rule out a different, not yet proposed, interstitial mechanism contributing to segregation in Fe–Cr–Ni alloys. Since the segregation predicted by vacancy effects alone tends to slightly overpredict the Ni-enrichment and Cr-depletion, any new proposed interstitial mechanism must bring Cr to the boundary faster than Ni.

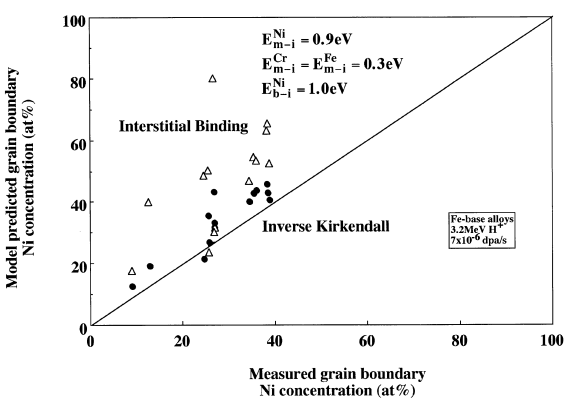

Fig. 7. Comparison of model predicted vs. measured grain boundary Ni concentration in Fe-base alloys. Open circles are Perks model predictions using inputs from Table 2. Open triangles are interstitial binding model calculations. For the interstitial binding model calculations, the interstitial migration and binding energies are listed.

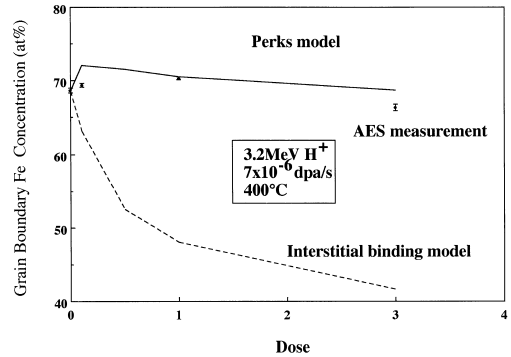

Fig. 8. Grain boundary Fe concentration in Fe–20Cr–9Ni irradiated at 400°C as a function of dose. Fe enriches at low (0 to 1.0 dpa) dose and depletes at high doses (> 3.0 dpa). The segregation measurements are compared to model calculations using (a) the Perks (inverse Kirkendall) model and (b) the interstitial binding model. Only the Perks model predicts the enrichment followed by depletion.

4.7. Comparison of the segregation of Fe in Fe–20Cr–9Ni to model predictions

The segregation of Fe in Fe–20Cr–9Ni is unique. From 0 to 1.0 dpa, Fe enriches at the grain boundary. From 1.0 to 3.0 dpa, Fe depletes at the boundary. At small doses, Fe diffuses slower than the alloy average and therefore enriches. At higher doses, the change in composition near the boundary result in Fe being a faster diffuser than the local average, causing Fe to deplete. This segregation behavior can be compared to both the Perks and the interstitial binding models.

Fig. 8 plots Fe segregation as a function of dose for Fe–20Cr–9Ni irradiated at 400°C, along with Perks model calculations using inputs from Table 2. The Perks model predicts an increase in the grain boundary Fe concentration at low dose followed by a depletion at higher dose. The dose dependence predicted by the Perks model does not exactly follow the dose dependence of the data (the model predicts a maximum Fe concentration at a lower dose), but enrichment followed by depletion is predicted as dose increases.

A comparison between the predictions of the interstitial binding model and the measured Fe segregation is shown in Fig. 8. The input parameters are the same as those used in Fig. 4 (specifically the input parameters from Table 2, with the exception of 0.3 eV for the interstitial migration energy for Fe and Cr, 0.9 eV for the interstitial migration energy of Ni, and 1.0 eV for the interstitial binding energy for Ni). The interstitial binding model does not predict *any* Fe enrichment. For all doses, the predicted Fe concentration is smaller than bulk values. Comparisons of the segregation behavior of Fe in irradiated Fe–20Cr–9Ni to both the Perks and the interstitial binding models again support vacancy transport as the primary segregation

mechanism in irradiated austenitic Fe–Cr–Ni alloys. The Perks model correctly predicts the trends in the segregation behavior of Fe, whereas the interstitial binding model does not.

In the previous sections, RIS data was analyzed in terms of segregation mechanisms. Specifically, the segregation data from proton-irradiated Fe–Cr–Ni alloys was analyzed with respect to both the Perks and the interstitial binding mechanisms. Segregation measurements as a function of composition and of temperature were analyzed and found to be consistent with a vacancy mechanism. However model predictions using the interstitial binding model resulted in poor agreement with the segregation measurements in the Fe-base alloys of this study. Predictions of the interstitial binding model agree with the RIS measurements only if unrealistic input parameters are used. Similarly, model predictions using a vacancy mechanism correctly predicted the change in Fe segregation in Fe–20Cr–9Ni, while the interstitial binding model did not. This detailed analysis of the segregation in proton irradiated Fe–Cr–Ni alloys indicates that RIS in these Fe–Cr–Ni alloys is sufficiently described using only a vacancy mechanism.

5. Segregation in neutron irradiated alloys

While a vacancy mechanism has been shown to be sufficient in describing the segregation in Fe–Cr–Ni alloys irradiated with protons, the mechanism should also describe the segregation in alloys irradiated with neutrons. In this section, the Perks and interstitial binding model calculations are compared to experimental results for alloys irradiated with neutrons to show the segregation is described adequately by a vacancy mechanism and that the interstitial binding model overpredicts the measured segregation.

Model predictions from the Perks and interstitial binding models can be compared to the segregation measurements from material irradiated with neutrons. Only a few studies of neutron irradiated material have examined the dependence of RIS in Fe–Cr–Ni alloys as a function of temperature and dose. The existing studies were summarized by Damcott et al. [17] and Allen and Was [34]. An examination of these studies indicate that the magnitude of the segregation is comparable in alloys with similar bulk composition irradiated with protons and neutrons. The magnitude of the segregation in 304 and 316 stainless steel alloys tends to be smaller than that in alloys with higher Ni concentration regardless of the irradiating particle. For example, the Ni segregation measurements of Norris et al. [9] from an Fe–20Cr–25Ni alloy irradiated at temperatures near 400°C are plotted as a function of dose in Fig. 9. The dose rate was not reported, so a dose rate of 5×10^{-8} dpa/s and an efficiency for producing freely migrating defects of 0.02 were used for model calculations [29]. For

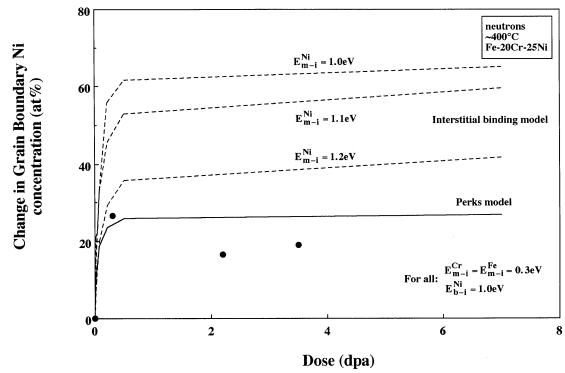

Fig. 9. Change in grain boundary Ni concentration in Fe–20Cr–25Ni [9], irradiated at 400°C with neutrons as a function of dose. Measurements are compared to model calculations using the Perks model and to the interstitial binding model. Perks model calculations use the inputs from Table 2. For the interstitial binding model calculations, the interstitial migration and binding energies are listed.

the Perks model calculations, the input parameters are those of Table 2. For the interstitial binding calculations, the input parameters are those of Table 2, except the interstitial binding energy is 1.0 eV for Ni and the interstitial migration energies are 0.3 eV for Fe and Cr. The Ni-interstitial migration energy is varied using three different values. As with the alloys irradiated with protons, the figure clearly shows that the Perks (vacancy effects) model is a much more accurate predictor of the measured segregation. The interstitial binding model predicts much greater segregation than measured, even using 1.2 eV for the Ni-interstitial binding energy, a value well outside the measured value of 0.89 ± 0.06 eV in Fe–16Cr–25Ni [37].

Several authors have measured segregation in 304 and 316 stainless steel alloys irradiated with neutrons at 288°C [12,39,40]. Fig. 10 shows a similar set of calculations for the Ni segregation in 304/316 stainless steel irradiated at 288°C to various doses. The input parameters for the model calculations are the same as in Fig. 9. While a Ni-interstitial migration energy of 1.2 eV gives model predictions as accurate as the Perks model, 1.2 eV is well outside the measured value for interstitial migration energy. Therefore, analysis of alloys irradiated with neutrons also indicates that the interstitial binding model does not accurately describe RIS in these Fe–Cr–Ni alloys. In analysis of materials irradiated with neutrons, the model calculations were compared to the Ni segregation because the interstitial binding model has a stronger effect on the Ni concentration than the Cr concentration.

For the interstitial binding model to be an accurate description of RIS in irradiated Fe–Cr–Ni alloys, the Ni segregation would have to be much larger than that seen in any measurement of grain boundary composition. This requirement was originally noted by Lam in calculations that included interstitial binding. Lam [35] observed that:

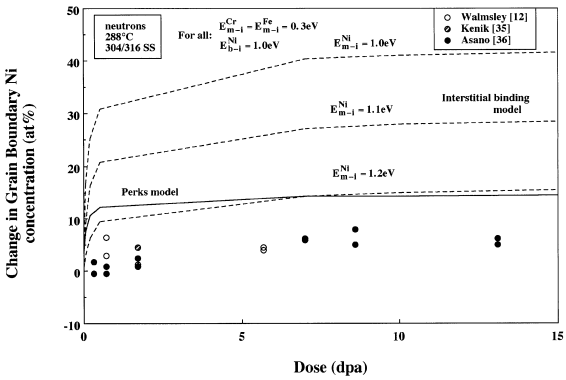

Fig. 10. Change in grain boundary Ni concentration in 304/316 stainless steel [12,39,40], irradiated at 288°C with neutrons as a function of dose. Measurements are compared to model calculations using the Perks model and to the interstitial binding model. Perks model calculations use the inputs from Table 2. For the interstitial binding model calculations, the interstitial migration and binding energies are listed.

Depending on driving forces, radiation-induced compositional changes can be slow or fast at a given temperature and damage rate. If vacancy fluxes are the only driving forces, segregation is small… On the other hand, if both vacancy and interstitial fluxes contribute to the segregation process, compositional redistribution is severe…

The segregation measurements from alloys using both protons and neutrons are consistent and show that segregation is best described using only vacancy effects.

6. Conclusions

Analysis of seven different Fe–Cr–Ni alloys indicates that RIS in Fe–Cr–Ni alloys is driven by the interaction with the vacancy flux and can be described by the inverse Kirkendall mechanism. Segregation measurements indicate that for Fe-base alloys, increasing the Cr concentration at constant Ni concentration causes the Cr to Fe diffusivity ratio to increase. For Fe-base alloys with constant Cr concentration, increasing the Ni concentration causes the Cr to Fe diffusivity ratio to decrease. Both trends are consistent with high temperature diffusion measurements, indicating that the segregation is driven by vacancy (inverse Kirkendall) effects. Additionally, each alloy has a maximum Cr depletion at a different temperature and therefore has a different vacancy migration energy. Since these migration energies are consistent with self-diffusion energies, the segregation is consistent with the inverse Kirkendall mechanism.

Analysis of Fe segregation in irradiated Fe–20Cr–9Ni also provides support for the inverse Kirkendall mechanism. The grain boundary Fe concentration in Fe–20Cr–9Ni irradiated at 400°C increases at low dose, then decreases at higher dose. This behavior is predicted by the inverse Kirkendall mechanisms but is not predicted by the interstitial binding model. The interstitial binding model, which preferentially couples Ni with the interstitial flux, predicts severe Fe depletion at the grain boundary at all doses.

The addition of interstitial binding effects to RIS models causes poor agreement between model predictions and segregation measurements in Fe–Cr–Ni alloys irradiated with protons or neutrons. Model calculations that include preferential binding of Ni to the interstitial flux lead to severe overpredictions of the measured Ni and Fe segregation. Model calculations that include interstitial binding can only be brought into agreement with RIS measurements by using unrealistic input parameters.

The primary mechanism causing segregation at grain boundaries in irradiated Fe–Cr–Ni alloys is the preferential participation of solute atoms with the vacancy flux. Additionally, the segregation kinetics for each alloy is unique. To accurately predict grain boundary segregation, alloy specific segregation kinetics must be *predicted* by the model. In a companion paper to this work, an inverse Kirkendall model has been developed which accurately describes RIS in Fe–Cr–Ni alloys of widely varying bulk compositions using a single set of parameters to describe atomic interactions [41].

Acknowledgements

The authors gratefully acknowledge P.L. Andresen at the General Electric for supplying the sample alloys and the bulk chemical analysis. We are grateful to J.M. Cookson and J. Gan for assistance in performing sample irradiations and to the Michigan Ion Beam Laboratory at the University of Michigan for the use of the irradiation facilities. We also thank the Surface Analysis Laboratory at the Ford Motor Research and Development Center for the use of their PHI 660 Scanning Auger Microprobes. Additional thanks go to the Electron Microbeam Analysis Laboratory and staff at the University of Michigan. Finally, thanks go out to S.M. Bruemmer at Pacific Northwest Laboratory for his support. This research was supported by the US Department of Energy under grant DE-FG02-93ER-12310, by the Associated Western Universities-Northwest under US Department of Energy grant DE-FG02-89ER-7552, and by the Southeast Universities Research Association through the SURA/ORNL summer research program. Research partially supported by the Division of Materials Sciences, US Department of Energy under contract DE-AC05-96OR22464 with Lockheed Martin Energy Research, and through the SHaRE Program under contract DE-AC05-76OR00033 with Oak Ridge Associated Universities. Partial support for T.R.A. was pro-

vided by a National Science Foundation Graduate Fellowship.

References

[1] P.R. Okamoto, L.E. Rehn, J. Nucl. Mater. 83 (1979) 2.
[2] P.L. Andresen, F.P. Ford, S.M. Murphy, J.M. Perks, in: Proc. 4th Int. Symp. on Environmental Degradation of Materials in Nuclear Power Systems—Water Reactors, Jekyll Island, GA, August 1989, NACE, Houston, 1990, p. 1.
[3] A.D. Marwick, R.C. Piller, M.E. Horton, in: Dimensional Stability and Mechanical Behaviour of Irradiated Metals, British Nuclear Energy Society, London, 1984, p. 11.
[4] J.M. Perks, A.D. Marwick, C.A. English, AERE R 12121, June 1986.
[5] H. Wiedersich, P.R. Okamoto, N.Q. Lam, J. Nucl. Mater. 83 (1979) 98.
[6] N.Q. Lam, A. Kumar, H. Wiedersich, in: H.R. Brager, J.S. Perrin (Eds.), Effects of Radiation on Materials: Eleventh Conference, ASTM STP 782, American Society for Testing and Materials, 1982, p. 985.
[7] A.J. Jacobs, in: A.S. Kumar, D.S. Gelles, R.K. Nanstad, E.A. Little (Eds.), Proc. 16th Int. Symp. on Radaition on Materials, ASTM-STP 1175, American Society for Testing and Materials, Philadelphia, 1993, p. 902.
[8] T. Kato, H. Takahashi, M. Izumiya, J. Nucl. Mater. 189 (1992) 167.
[9] D.I.R. Norris, C. Baker, C. Taylor, J.M. Titchmarsh, in: R.E. Stoller, A.S. Kumar, D.S. Gelles (Eds.), Effects of Radiation on Materials: 15th International Symposium, ASTM STP 1125, American Society for Testing and Materials, 1992, p. 603.
[10] K. Nakata, I. Masaoka, J. Nucl. Mater. 150 (1987) 186.
[11] S.M. Bruemmer, L.A. Charlot, E.P. Simonen, in: Proc. Seventh Int. Symp. on Env. Deg. of Materials in Nuclear Power Systems—Water Reactors, NACE, Breckenridge, CO, 1995, p. 971.
[12] J. Walmsley, P. Spellward, S. Fisher, A. Jenssen, in: Proc. Seventh Int. Symp. on Env. Deg. of Materials in Nuclear Power Systems—Water Reactors, NACE, Breckenridge, CO, 1995, p. 985.
[13] S. Dumbill, PhD thesis, University of Birmingham, 1992.
[14] S. Dumbill, T.M. Williams, in: Proceedings of the Conference on Materials for Nuclear Reactor Core Applications, BNES, London, Vol. 1, 1987, p. 119.
[15] S. Watanabe, H. Kinoshita, N. Sakaguchi, H. Takahashi, J. Nucl. Mater. 226 (1995) 330.
[16] S.M. Bruemmer, in: I.M. Robertson, L.E. Rehn, S.J. Zinkle, W.J. Pythian (Eds.), Proceedings of the MRS Fall Meeting: Symposium Y: Microstructure of Irradiated Materials, Vol. 373, 1995, p. 119.
[17] D.L. Damcott, T.R. Allen, G.S. Was, J. Nucl. Mater. 225 (1995) 97.
[18] D.L. Damcott, G.S. Was, S.M. Bruemmer, in: I.M. Robertson, L.E. Rehn, S.J. Zinkle, W.J. Phythian (Eds.), Proceedings of the MRS Fall Meeting Symposium Y: Microstructure of Irradiated Materials, Vol. 373, 1995, p. 131.
[19] E.P. Simonen, L.A. Charlot, S.M. Bruemmer, J. Nucl. Mater. 225 (1995) 117.
[20] R.D. Carter, D.L. Damcott, M. Atzmon, G.S. Was, S.M. Bruemmer, E.A. Kenik, J. Nucl. Mater. 211 (1994) 70.
[21] T.R. Allen, D.L. Damcott, G.S. Was, E.A. Kenik, in: Proc. Seventh Int. Symp. on Env. Deg. of Materials in Nuclear Power Systems—Water Reactors, NACE, Breckenridge, CO, 1995, p. 997.
[22] M.J. Norgett, M.T. Robinson, I.M. Torrens, Nucl. Eng. Des. 33 (1974) 50.
[23] S.J. Rothman, L.J. Nowicki, G.E. Murch, J. Phys. F. 10 (1980) 383.
[24] J.M. Perks, A.D. Marwick, C.A. English, in: Proceedings of the Symposium on Radiation-induced Sensitization of Stainless Steels, Berkeley Nuclear Laboratories, 23 September 1986, CEGB, Berkeley Nuclear Laboratories, Berkeley, Gloucestershire, 1987.
[25] R.W. Seigel, in: H. Takamura (Ed.), Point Defects and Interactions in Metals, North-Holland, Amsterdam, p. 533.
[26] M. Kiritani, H. Tanaka, J. Nucl. Mater. 69&70 (1978) 277.
[27] C. Dimitrov, O. Dimitrov, J. Phys. F. 14 (1984) 793.
[28] R.D. Carter, D.L. Damcott, M. Atzmon, G.S. Was, E.A. Kenik, J. Nucl. Mater. 205 (1993) 361.
[29] G.S. Was, T. Allen, J. Nucl. Mater. 205 (1993) 332.
[30] M.P. Seah, W.A. Dench, Surf. Interface Anal. 1 (1979) 2.
[31] S. Watanabe, H. Takahashi, J. Nucl. Mater. 208 (1994) 191.
[32] J. Ruzickova, B. Million, Mater. Sci. Eng. 50 (1981) 59.
[33] B. Million, J. Ruzickova, J. Vrestal, Mater. Sci. Eng. 72 (1985) 85.
[34] T.R. Allen, G.S. Was, J. Nucl. Mater. 244 (1997) 278.
[35] N.Q. Lam, J. Nucl. Mater. 117 (1983) 106.
[36] F.W. Young, J. Nucl. Mater. 69&70 (1978) 310.
[37] O. Dimitrov, C. Dimitrov, J. Nucl. Mater. 105 (1982) 39.
[38] P.H. Dederichs, C. Lehmann, H.R. Schober, A. Scholz, R. Zeller, J. Nucl. Mater. 69&70 (1978) 176.
[39] E.A. Kenik, J. Nucl. Mater. 187 (1992) 239.
[40] K. Asano, K. Fukuya, K. Nakata, M. Kodoma, in: Proceedings of the Fifth International Symposium on Environmental Degradation of Materials in Nuclear Power Systems—Water Reactors, American Nuclear Society, Monterey, CA, 1992, p. 838.
[41] T.R. Allen, G.S. Was, Acta Metall., in press.